

# Interplay between Growth Mechanism, Materials Chemistry, and Band Gap Characteristics in Sputtered Thin Films of Chalcogenide Perovskite BaZrS<sub>3</sub>

Soham Mukherjee,\* Stefania Riva, Corrado Comparotto, Fredrik O. L. Johansson, Gabriel J. Man, Dibya Phuyal, Konstantin A. Simonov, Justus Just, Konstantin Klementiev, Sergei M. Butorin, Jonathan J. S. Scragg, and Håkan Rensmo\*

Cite This: *ACS Appl. Energy Mater.* 2023, 6, 11642–11653

Read Online

ACCESS |

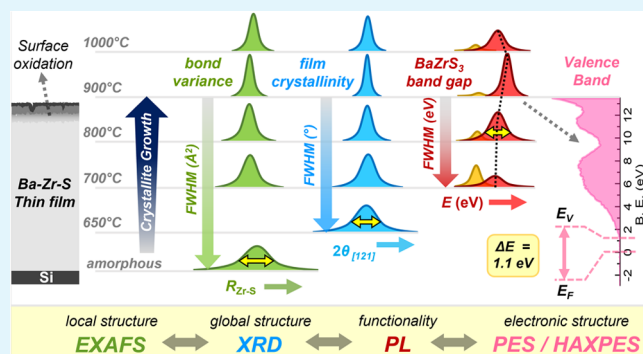
Metrics & More

Article Recommendations

Supporting Information

**ABSTRACT:** The prototypical chalcogenide perovskite BaZrS<sub>3</sub>, characterized by its direct band gap, exceptionally strong light-harvesting ability, and good carrier transport properties, provides fundamental prerequisites for a promising photovoltaic material. This inspired the synthesis of BaZrS<sub>3</sub> in the form of thin films, using sputtering and rapid thermal processing, aimed at device fabrication for future optoelectronic applications. Using a combination of short- and long-range structural information from X-ray absorption spectroscopy (XAS) and X-ray diffraction (XRD), we have elucidated how, starting from a random network of Ba, Zr, and S atoms, thermal treatment induces crystallization and growth of BaZrS<sub>3</sub> and explained its impact on the observed photoluminescence (PL) properties. We also provide a description of the electronic structure and substantiate the surface material chemistry using a combination of depth-dependent photoelectron spectroscopy (PES) using hard X-ray (HAXPES) and traditional Al K<sub>α</sub> radiation. From the knowledge of the optical band gap of BaZrS<sub>3</sub> thin films, synthesized at an optimal temperature of 900 °C, and our estimation of the valence band edge position with respect to the Fermi level, one may conclude that these semiconductor films are intrinsic in nature with a slight *n*-type character. A detailed understanding of the growth mechanism and electronic structure of BaZrS<sub>3</sub> thin films helps pave the way toward their utilization in photovoltaic applications.

**KEYWORDS:** chalcogenide perovskites, BaZrS<sub>3</sub>, EXAFS, XRD, structure–property correlation, photoelectron spectroscopy, HAXPES



## INTRODUCTION

The term “chalcogenide perovskite” (CP) refers to the family of perovskites (chemical formula ABX<sub>3</sub>), where the anion (X) site is usually occupied by high atomic number chalcogens (S or Se), while the A and B sites are typically occupied by alkaline earths (group II A elements: Ba or Sr) and group IV B elements (Hf or Zr), respectively. Although CPs have been known since the late 1950s,<sup>1,2</sup> the recent renewed interest in these materials stems from their potential for photovoltaic<sup>3–5</sup> and thermoelectric applications.<sup>6–8</sup> In photovoltaic research, the power conversion efficiency of the related halide perovskite solar cells has skyrocketed over the past decade.<sup>9</sup> However, due to their hybrid organic–inorganic framework, these perovskites suffer from inherent instability toward exposure to moisture, heat, and electric fields.<sup>9,10</sup> Furthermore, the presence of toxic elements, such as lead, renders them less suitable for environmentally friendly applications. In contrast, the relatively less explored all-inorganic CPs, characterized by a large

absorption coefficient, offer hope for the realization of a more stable, nontoxic (Pb-free) alternative.

Within the CP family, BaZrS<sub>3</sub> possesses a good carrier mobility of 2.1 to 13.7 cm<sup>2</sup>/(Vs)<sup>11</sup> at room temperature and a direct band gap of ca. 1.7–1.85 eV,<sup>4,12</sup> which lies in close proximity to the optimal range for the upper absorber in a tandem solar cell.<sup>13,14</sup> This prototypical semiconductor is characterized by a large absorption coefficient<sup>12,15,16</sup> (>10<sup>5</sup> cm<sup>-1</sup>) near edge, caused by intense *p*–*d* interband transition<sup>17–19</sup> from high-density S 3*p* valence states to unoccupied S 3*d* and empty cationic *d* states (Ba 5*d*, Zr 4*d*) in the conduction band. Such enhanced mixing of states

**Received:** August 18, 2023  
**Revised:** October 29, 2023  
**Accepted:** October 30, 2023  
**Published:** November 14, 2023



between Ba, Zr, and S is a direct consequence of the higher covalency of S compared to O, rendering the BaZrO<sub>3</sub> counterpart to be electrically insulating (3.9 eV).<sup>17</sup>

Another key aspect is the perovskite structure of BaZrS<sub>3</sub>, where the degree of cooperative tilting between the corner-shared arrangement of Zr–S<sub>6</sub> octahedral units spaced out by Ba atoms in a three-dimensional lattice controls the band gap.<sup>19,20</sup> Specifically, BaZrS<sub>3</sub> assumes an orthorhombic structure (space group *Pnma*<sup>21</sup>) exhibiting classical GdFeO<sub>3</sub>-type distortion.<sup>22</sup> This leads to antipolar cationic displacements<sup>5</sup> and buckling of Zr–S–Zr bond angle to be inequivalent along all three crystallographic axes, thereby making the system intrinsically nonpolar. Chalcogens with higher covalent character (S, Se, and Te), when coupled with this structural anisotropy, make these semiconductors highly polarizable and facilitate strong polaron transport effects along specific lattice directions. The low-frequency relative dielectric constant, which controls the magnitude of band bending and hence charge redistribution at semiconductor junctions, has been reported to be ca. 50–100 for BaZrS<sub>3</sub>.<sup>3</sup>

The distorted perovskite structure, while beneficial for charge transport, strongly hinders ion migration, making the system extremely robust to degradation against oxidation, moisture, light,<sup>23</sup> and heat.<sup>24</sup> The remarkable stability of BaZrS<sub>3</sub> is evident from its capability to withstand rather high hydrostatic pressures up to 8.9 GPa,<sup>25</sup> allowing band gap engineering with a wide chemical pressure range through site-selective doping.<sup>26–28</sup> Theoretical calculations<sup>15,16,29</sup> have projected a maximum efficiency of 38.7% for a CP/crystalline Si tandem architecture<sup>18</sup> using optimized Ba(Zr,Ti)S<sub>3</sub>. Moreover, all three constituent elements (Ba, Zr, and S) have high earth abundance,<sup>12</sup> highlighting the potential for scalable manufacturing.

However, a prerequisite for enabling large-scale device fabrication lies in the possibility that the material can be grown in a thin film configuration. This step is crucial, as such dimensionality reduction<sup>30,31</sup> often leads to band gap alteration in perovskites. This need directed recent efforts toward the synthesis of BaZrS<sub>3</sub> thin films<sup>11,23,32,33</sup> using different techniques than bulk synthesis,<sup>34–36</sup> including our first report of BaZrS<sub>3</sub> thin films fabricated using the sputtering technique.<sup>37</sup> The resulting films exhibited the best optical response at an optimal annealing temperature of 900 °C with crystal quality comparable to that from bulk synthesis methods.

In this paper, we have investigated the nature of the reported thin films in terms of their geometric structure, phase distribution, surface, and near-surface chemical and electronic structures, and how they correlate to the optical absorption and band gap data.<sup>37</sup> More specifically, linking extended X-ray absorption fine structure spectroscopy (EXAFS) as the state-of-the-art local structural probe to complementary long-range structural information from XRD, we have followed the temperature dependence of crystallization and the reaction sequence of material formation. The corresponding electronic structure at each step of the growth mechanism is revealed by X-ray photoelectron spectroscopy (XPS). Using depth-dependent hard X-ray photoelectron spectroscopy (HAXPES), we also provide a description of the electronic structure of the thin films prepared at 900 °C, which exhibits the highest degree of crystallinity. A detailed understanding of the growth mechanism, bulk, and surface electronic structures of BaZrS<sub>3</sub> thin films will contribute to utilizing such films in photovoltaic applications. Such knowledge is also key to evaluating the

applicability of BaZrS<sub>3</sub> for thermoelectric and other optoelectronic devices.

## ■ EXPERIMENTAL SECTION

**Sample Preparation.** Films of BaZrS<sub>3</sub> were prepared by reactive co-sputtering of Ba–Zr–S “precursor” films at ambient temperature, followed by a thermal treatment to induce crystallization. Sputtering was carried out using a BaS and a Zr target in H<sub>2</sub>S-containing atmosphere. Because of different constraints in terms of process temperature and time, two different furnaces were used to vary the thermal treatment conditions. For the low temperature (650 °C), the sample was annealed in a custom-made tube furnace for 20 min in Ar atmosphere. The other samples were annealed in a rapid thermal processor (RTP) for 1 min in N<sub>2</sub> atmosphere (no S was allowed), and the temperature was varied from 700 to 1000 °C. After annealing, cracks and pinholes were present in the films. The precursors are hereafter referred to as BZS-pre, and the annealed films correspond to the annealing temperature: BZS-650, BZS-700, BZS-800, BZS-900, and BZS-1000. A detailed description of the sample preparation can be found in our previous paper.<sup>37</sup>

Although it uses rather high temperatures from the point of view of a solar cell fabrication, the synthesis process of the samples described here is instructive because it represents a pure crystallization of BaZrS<sub>3</sub> from an initially amorphous precursor, without intermediates or substantial contributions of secondary phases. Therefore, the results can be directly correlated to the fundamental bonding properties of this material. Subsequent synthetic development has taken place, leading to much lower temperature growth routes, where the film is grown in a multistage process via intermediates.<sup>33</sup> The results presented here for the pure crystalline BaZrS<sub>3</sub> phase (under the optimal growth conditions) are of relevance regardless of the growth route.

**XAS.** X-ray absorption spectroscopy (XAS) measurements at the Zr *K*-edge were performed at the BALDER beamline<sup>38</sup> in MAX IV, Lund, Sweden, with high photon flux (10<sup>12</sup> photons/sec) and high resolution ( $\Delta E/E \sim 2 \times 10^{-4}$ ). The incident photon beam was monochromatized by using a Si (111) double-crystal monochromator; the high harmonics were reduced by two mirror reflections. A mixture of nitrogen and helium gas was optimized to absorb ca. 5–10% of the incident photons in the first ionization chamber measuring the incident flux. Ba–Zr–S films were oriented at 45° with respect to the incident X-ray beam, thereby allowing the simultaneous measurement of a reference foil using the transmitted beam intensity. Fluorescence data were collected by using a 7-element SDD detector. The amplitude loss in the fluorescence data due to self-absorption effects was found to be small and was corrected using the Booth algorithm.<sup>39</sup> During the data collection, multiple scans were recorded for each sample. Comparing these individual scans against their average gives an idea of the noise level and the reliability of the data. Data processing and analyses were performed using the Athena-Artemis software suite, a front end to FEFF and IFEFFIT.<sup>40</sup> The subtracted background was calculated using the AUTOBK algorithm implemented in the software.<sup>41</sup>

**XPS.** XPS measurements were performed on as-prepared samples mounted on copper stubs with a silver paste, using monochromatic Al *K*<sub>α</sub> radiation (1.487 keV) with an output energy of 25 W (15 kV) in a commercial photoelectron spectrometer PHI Quantera II from Physical Electronics. The base pressure of the chamber was maintained around  $5 \times 10^{-10}$  mbar during the experiments. For the analysis of the XPS spectra, in terms of contributions from individual components representing different species, experimental spectra were fitted by a combination of components by minimizing the total squared error (least-squared-error) of the fit. Individual components were represented by a convolution of the Lorentzian function and a Gaussian function to account for the instrumental resolution. A combination of the linear and Shirley background functions was considered to account for the inelastic background in the XPS spectra. All of the survey spectra were acquired with a pass energy of 224 eV and an energy step of 0.8 eV, while the core levels were measured with

a pass energy of 55 eV and an energy step of 0.1 eV. The energy calibration of all of the spectra was done based on the subsequent measurements at the higher probing energy of 4.0 keV.

**HAXPES.** Hard X-ray PES (HAXPES) was carried out at BESSY II (Helmholtz Zentrum Berlin, Germany) at the KMC-1 beamline using the HIKE end-station,<sup>42</sup> which provides a tunable photon energy range from 2 to 12 keV that can be selected using a double-crystal monochromator (Oxford-Danfysik). The photoelectron kinetic energies (KE) were measured by using a VG Scienta R4000 electron energy analyzer optimized for high kinetic energies. In this work, a photon energy of 4.0 keV was used by selecting first-order light from a Si (311) crystal. The pressure in the analysis chamber was  $\sim 10^{-8}$  mbar. A pass energy of 200 eV was used for acquiring the overview spectra, core-level peaks and the valence band spectra. The HAXPES spectra presented in this work were energy calibrated versus the Fermi level at zero binding energy, which was determined by measuring a gold plate in electrical contact with the sample and setting the Au 4f<sub>7/2</sub> core-level peak to 84.0 eV. On the basis of this measurement, the overall resolution in the HAXPES measurements was lower than 0.5 eV. Elemental composition analyses were performed by integrating the areas under respective elemental peaks corrected for cross section, which gives the atomic fraction of each element.

## RESULTS

**XAS.** Figure 1(a) shows the normalized X-ray absorption near-edge spectroscopy (XANES) data for the Zr K-edge for

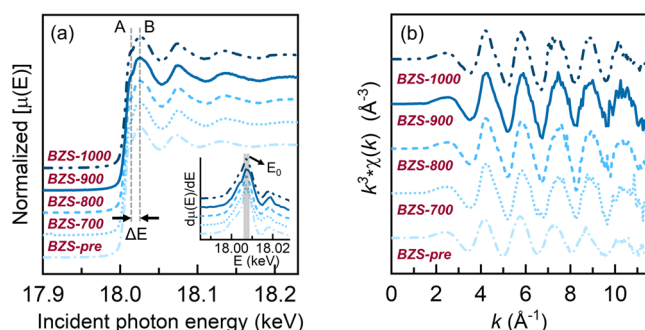


**Figure 1.** Evolution of (a) Zr K-XANES for freshly sputtered Ba–Zr–S thin films (amorphous; light blue) and films annealed at increasing annealing temperatures (the darker the blue, the higher the annealing temperature); the inset shows the corresponding first derivatives. (b) The corresponding  $k^3$ -weighted  $\chi(k)$  functions for Zr K-XAS data.

the Br–Zr–S precursor and annealed films; the corresponding first derivatives are shown as the inset in Figure 1(a). The absorption energy positions ( $E_0$ ) were estimated from the maxima of the inflection in the dominant region of the XANES derivatives (energy range marked by the shaded region in the inset of Figure 1(a)). The average  $E_0$  value is  $18006.7 \pm 0.35$  eV, similar to the reported value for Zr in  $\text{ZrO}_2$ .<sup>43</sup> The spread of  $E_0$  values is also rather narrow ( $<1$  eV), indicating that Zr exists predominantly as  $\text{Zr}^{4+}$  in the sputtered films.<sup>43</sup> The presence of features A and B above the  $E_0$  position (vertical dashed lines in Figure 1(a)) gives a qualitative diagnostic for the average coordination environment of Zr close to six. However, the peaks are broad with an energy splitting ( $\Delta E \sim 9$  eV) lower than the standard 6-fold<sup>44</sup> coordination of Zr in a regular octahedral geometry ( $\text{BaZrO}_3$ ). The Zr sites are thus expected to assume a lower degree of centrosymmetry, which yields a higher disorder in the local environment around Zr.

Figure 1(b) shows how the  $k^3$ -weighted  $\chi(k)$  functions for Zr K-edge data evolve when sputtered Br–Zr–S films are annealed at different temperatures. From the overall resemblance of the

$\chi(k)$  oscillations for the as-deposited and annealed Ba–Zr–S films, one expects similarities in the Zr environments in all samples. The main difference lies in the  $\chi(k)$  amplitude, which is noticeably lowest for the precursor film (BZS-pre), with the  $\chi(k)$  definition getting poorer at relatively low wave numbers ( $k_{\text{max}} \sim 10.0 \text{ \AA}^{-1}$ ). With annealing (700 °C), an immediate increase of the  $\chi(k)$  amplitude is observable, with the  $\chi(k)$  definition improving to higher wave numbers ( $k_{\text{max}} \sim 11.5 \text{ \AA}^{-1}$ ). Further annealing up to 900 °C leads to slightly larger, albeit comparable,  $\chi(k)$  amplitudes, with no perceivable increase of the  $k_{\text{max}}$  values. A small dampening of the  $\chi(k)$  functions is noticeable at 1000 °C, particularly at above  $10.0 \text{ \AA}^{-1}$ , most likely related to interference from the Zr local environment in  $\text{ZrO}_2$ , which reportedly forms at this temperature.<sup>37</sup> Figure 2(a) compares the  $\chi(R)$  or  $R$ -space,

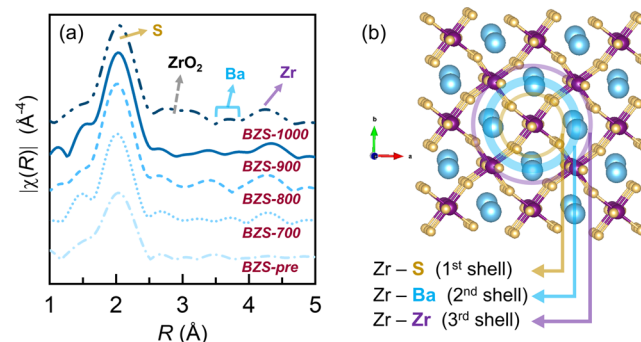


**Figure 2.** (a) Evolution of modulus of the  $\chi(R)$  functions for Zr K-edge data for freshly sputtered (amorphous; light blue) and annealed Ba–Zr–S thin films at increasing annealing temperatures (the darker the blue, the higher the annealing temperature). (b) Schematic of  $\text{BaZrS}_3$  perovskite structure in orthorhombic symmetry and spatial distribution of Ba, Zr, and S coordination shells within the three-dimensional lattice.

i.e., modulus of the Fourier transformation of the  $\chi(k)$  functions (Figure 1(b)) for the Zr K-edge data of all Ba–Zr–S films. A schematic representation of the  $\text{BaZrS}_3$  perovskite structure ( $\text{ABX}_3$ ) in orthorhombic symmetry is given in Figure 2(b). The spatial distributions of the near neighboring (NN) coordination shells: first-shell S atoms (1NN; X site: yellow), second-shell Ba atoms (2NN; A site: blue), and third-shell Zr atoms (3NN; next B site: purple) surrounding a central Zr atom (B site) is highlighted. The different NN shells within the Zr local structure (1NN: 6S, 2NN: 8Ba, 3NN: 6Zr) are correlated to their positions in the  $\chi(R)$  data (Figure 2(a)). The interatomic distance values are underestimated due to the phase shifts of the different atomic-pair correlations that were accounted for during the fitting procedures, as elaborated in the Supporting Information. The first-shell peak occurring at  $R \sim 2.0 \text{ \AA}$  (Figure 2(a)) corresponds to 6 S (X site: yellow), with possible contributions from O due to surface oxidation.<sup>37</sup> The peaks in the  $R$  range 3–4 Å correspond to scattering from the 8 Ba (A site: blue), whereas the peak around  $R \sim 4.2 \text{ \AA}$  corresponds to scattering from the 6 Zr (B site: purple) including multiple scattering contributions from Zr–Zr–S paths.

The higher shell peaks in Zr K-  $\chi(R)$  are practically nonexistent in the precursor film, suggesting that the Zr–Zr and Zr–Ba correlations do not attain a long-range order. However, after annealing at 700 °C, these correlations start emerging, gaining intensity in the temperature range of 800–

900 °C. At 1000 °C, the Zr  $K$ - $\chi(R)$  function shows slight modifications due to additional contributions from secondary phases related to sample decomposition, primarily ZrO<sub>2</sub>. This can be identified from the emergence of characteristic Zr–Zr correlations (marked in Figure 2(a)) occurring in ZrO<sub>2</sub>. The increase of the 1NN peak amplitude upon annealing the Ba–Zr–S precursor film up to 900 °C indicates that the S environment around Zr is becoming less distorted. The higher shell peaks appear smoother, indicating that the distribution of interatomic distances probably becomes more disordered rather than assuming a characteristic distorted structure with distinct bond lengths. The Zr–Zr correlations appear more distinct compared to Zr–Ba correlations, which suggests that Ba atoms assume a spatial distribution larger than that of the adjacent Zr atoms. Such arrangement is typical of the GdFeO<sub>3</sub>-type orthorhombic distortion, which splits the A site into four equivalent sites, thereby creating a 4 × 2 distribution of Zr–Ba correlations that will interfere and lower the  $\chi(R)$  amplitude (see Figure 2). Nonetheless, the dampening effect is still significant considering the high scattering probabilities of Ba and Zr and possibly includes contributions from size effects.

The  $\chi(R)$  amplitude falls off as  $1/R^2$ , so most distinct local structural changes are visible in the first peak, as compared to higher shell peaks in the  $\chi(R)$ . It is evident from Figure 2(a) that the 1NN  $\chi(R)$  amplitude of the Ba–Zr–S precursor is significantly lower compared to the annealed films, which could arise from undercoordination of S to Zr, high disorder, or size effects. Since the as-deposited films are amorphous, one finds high disorder in the immediate local geometry surrounding Zr, rendering  $k_{\max}$  to be low (Figure 1(b)). Annealing at 700 °C improves the short-range order in the local environment around Zr, increasing the  $k_{\max}$  value and leading to a sharp increase of the  $\chi(R)$  amplitude. Annealing at higher temperatures (800–900 °C) still improves the short-range order, but the changes are relatively smaller, leading to a smaller increase in  $\chi(R)$  amplitudes. The  $\chi(R)$  intensity slightly decreases at 1000 °C and is most likely due to lower scattering contribution from the O coming from ZrO<sub>2</sub>. The Zr  $K$ -XAFS data were modeled both for 1NN and higher NN features. However, we would focus our discussions more on the results from 1NN, the dominant contributor to the total EXAFS signal. From our comparative EXAFS analyses on all of the films, we find that the O contribution in the Zr signal is appreciable only for the precursor sample and the films annealed at 1000 °C, allowing us to estimate the O content independently. For the remaining films, an independent estimation of O was unreliable, suggesting that the O contribution to the 1NN EXAFS was negligible compared to the S contribution. An increase of the O coordination of the atoms around Zr at 1000 °C becomes apparent due to the formation of ZrO<sub>2</sub> detected with XRD, this being beyond the formation temperature of BaZrS<sub>3</sub> (900 °C). The details of the fitting approach, extracted parameters, and error analyses are provided in the Supporting Information. Figure S1(a,b) and Table S1 compare 1NN fits to the Zr  $K$ - $\chi(R)$  data for BZS-pre without and with O contribution, while Figure S1(c) and Table S2 compare 1NN fits to the real part of the Zr  $K$ - $\chi(R)$  functions and the corresponding magnitudes of  $\chi(R)$  for the entire series of Ba–Zr–S thin films.

The amplitude reduction factor, which accounts for multiple electron excitation losses at the absorbing atom, was estimated as an empirical parameter and was used as a constant scaling factor during the EXAFS analysis for the entire series. This

allows a direct comparison of coordination numbers among different films, ruling out the influence of the amplitude reduction factor on  $\chi(R)$  amplitudes. In Figure 3(a), we plot

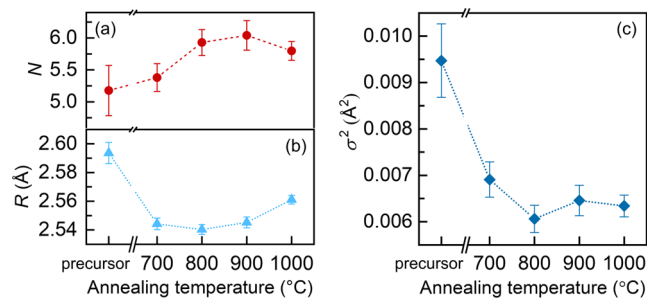


**Figure 3.** (a) Average coordination number ( $N$ ) of S bonded to Zr, (b) average Zr–S bond distances ( $R$ ), and (c) pseudo-Debye–Waller factors ( $\sigma^2$ ) for the Zr–S pair obtained from Zr  $K$ -EXAFS analyses.

the number of S atoms ( $N$ ) coordinated to Zr during the crystallization process. One can clearly see an undercoordination of S (Zr–S coordination  $<6$ ) for the precursor film. As the films are annealed, an immediate increase of the S coordination number is observed. The number systematically increases with increasing temperature until it approaches the ideal octahedral Zr coordination in the orthorhombic BaZrS<sub>3</sub> at 900 °C. Going from 900 to 1000 °C, the S coordination decreases slightly.

The corresponding average Zr–S bond distances ( $R$ ) are plotted in Figure 3(b). We find the average Zr–S distances to be the largest for precursors. With annealing, a decrease in the Zr–S bond length is observed in the temperature range 700–900 °C, assuming distances proximal to the ideal value for Zr–S bonds (ca. 2.53–2.54 Å) in orthorhombic BaZrS<sub>3</sub>. Going from 900 to 1000 °C, the Zr–S distances increased slightly. We mention here that, although orthorhombic structure can lead to a 2 + 2 + 2 spatial distribution of Zr–S bonds, such distortions, if present, were too small to be resolved in  $\chi(R)$ . A better description was obtained using a single Zr–S distance, with the information on the distribution width contained in the pseudo-Debye–Waller factors ( $\sigma^2$ ) for the Zr–S pair. The  $\sigma^2$  parameter, therefore, is essentially an indicator of the extent of structural disorder in the films. All extracted  $\sigma^2$  values for the Zr–S pair in Ba–Zr–S films are plotted in Figure 3(c). The Zr–S  $\sigma^2$  value is the largest for the precursor films. With annealing, it drops significantly until 800 °C, beyond which  $\sigma^2$  seems to increase marginally but at a slower rate. Films annealed at 1000 °C, however, are characterized by a lower coordination number and longer Zr–S bonds, suggesting a deviation from the BaZrS<sub>3</sub> structure. This is related to the onset of decomposition of the BaZrS<sub>3</sub> structure, which creates secondary phases. The higher uncertainties for local parameters ( $R$ ,  $N$ , and  $\sigma^2$  in Figure 3) extracted for BZS-pre are related to the amorphous nature of the film.

The XRD profiles for annealed Ba–Zr–S thin films (650 to 1000 °C) and full width at half-maximum (FWHM) values are already reported.<sup>37</sup> In Figure 4(a), we focus on the most intense Bragg peak ([121] reflection at  $2\theta \sim 25.3^\circ$ ) of the XRD profiles and track the temperature evolution of the FWHM of the [121] peak ( $[121]_{\text{FWHM}}$ ). This allows us to extract crucial structural information, e.g., lattice parameters, film crystallinity, and average crystallite size, and show how these parameters change with annealing over the temperature range of 650 to 1000 °C. The  $[121]_{\text{FWHM}}$  values (dark red

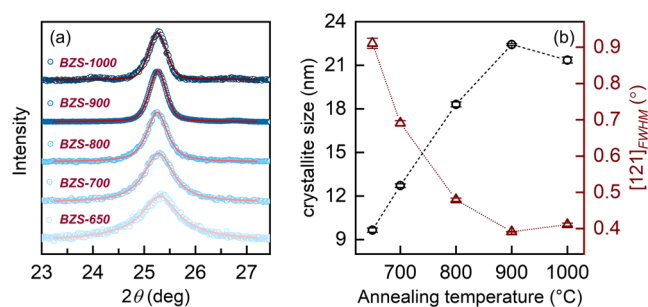


**Figure 4.** (a) Detailed view of the [121] Bragg reflection of the annealed Ba–Zr–S films. (b) Evolution of crystallite size in nanometers and [121]<sub>FWHM</sub> in degrees, extracted from the XRD fits in (a).

open triangles, right axis of Figure 4(b)) estimated from single pseudo-Voigt function fits to the [121] Bragg peaks show a monotonic decrease from 650 °C up to 900 °C, followed by a slight increase at 1000 °C. The sharper the Bragg reflection, the more well defined are the positions of different atoms constituting that atomic plane. Narrowing of the [121]<sub>FWHM</sub> therefore indicates improved extent of crystallinity upon annealing from 650 °C up to 900 °C and is a direct consequence of the temperature-induced growth of BaZrS<sub>3</sub> crystallites. The average crystallite sizes extracted using the Scherrer fits are shown in Figure 4(b) (black open circles, left axis), revealing the largest crystallite size for the BZS-900 film. During this entire process of temperature-induced BaZrS<sub>3</sub> crystallization and growth, the position of the [121] Bragg peaks remain rather consistent, ranging only between  $2\theta \sim 25.31$  for 650 °C to  $2\theta \sim 25.25$  1000 °C, indicating no appreciable temperature effect on the unit cell parameters.

Large crystallite sizes for BZS-900 and BZS-1000 prompted us to extend our EXAFS fits to higher NN shells for these films. Although low amplitudes of higher NN shells in Zr  $K$ - $\chi(R)$  render larger uncertainties to the fit parameters, we find that the average Zr–Ba and Zr–Zr (2NN and 3NN, respectively, Figure 2(b)) interatomic distances for BZS-900 are close to the reported orthorhombic crystal structure.<sup>21,22</sup> A similar observation holds for BZS-1000, where the EXAFS model included contributions from cubic ZrO<sub>2</sub> as well and was fit up to 2NN. The higher NN fits to the magnitude of the  $\chi(R)$  functions for Zr  $K$ -XAS data of BZS-900 and BZS-1000, and the individual contributions of the dominant scattering paths are shown in Figure S2 in the Supporting Information, alongside the detailed fitting procedure and the extracted parameters (Table S3). Parameters extracted from XRD analyses include position ( $2\theta$ ) and FWHM (deg) for the [121] Bragg reflection, and average BaZrS<sub>3</sub> crystallite size (nm) present in different BZS thin films, which are compared in Table S4. We notice a clear parallel between the evolution of the [121]<sub>FWHM</sub> from XRD and the evolution of Zr–S  $\sigma^2$  from EXAFS with an increase of annealing temperature, revealing good agreement between structural descriptions obtained at global (XRD) and local (EXAFS) probe lengths, which will be considered further in the Discussion section.

**XPS.** The chemical and electronic structures for all Ba–Zr–S films were characterized by using XPS, a surface-sensitive analysis technique used to obtain information on elemental species, composition, and chemical state on the surface through the detection of photoelectrons emitted by irradiating the sample with X-rays. The sensitivity can vary on the order of

0.5–5 nm, depending on the excitation source. This is of particular interest from a materials fabrication perspective since the surface of the film contributes to the properties of subsequent interfaces in a multilayer device like a solar cell.

Elemental contents in the surface layers of the sputtered Ba–Zr–S thin films were evaluated by Al  $K_{\alpha}$  XPS (1.487 keV). A survey scan was taken to identify all of the material core levels, valence band, and impurities. Figure 5 compiles (a) a

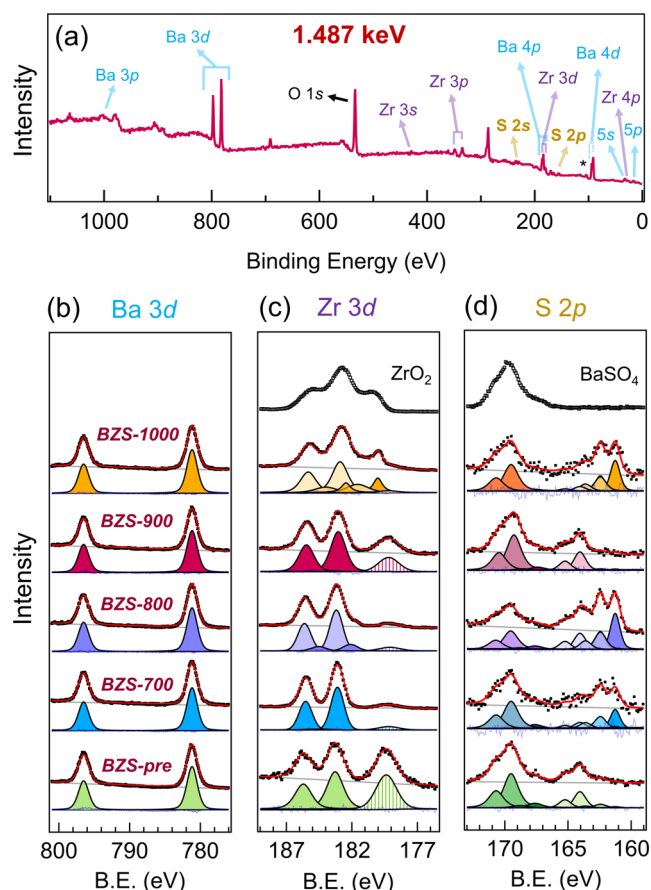


**Figure 5.** Al  $K_{\alpha}$  XPS: (a) Survey scan of Ba–Zr–S thin films annealed at 900 °C with different core-level peaks identified. Data (black symbols) and fit (red) to core-level spectra for (b) Ba 3d, (c) Zr 3d, and (d) S 2p data for all Ba–Zr–S thin films. The individual components for each fit for the Ba 3d, Zr 3d, and S 2p data are also presented.

survey scan (BZS-900 film), with core-level contributions identified, and (b) Ba 3d, (c) Zr 3d, and (d) S 2p core-level spectra, comparing the amorphous precursor films with those annealed at increasing temperatures. The data (black symbols), fit (red lines), and components for each fit are also given for the respective core-level spectra.

The Ba 3d and Zr 3d doublets appear with characteristic spin–orbit splitting of 15.33 and 2.43 eV, respectively, consistent with the oxidation states of Ba and Zr being +2 and +4, respectively, as expected for a perovskite structure.<sup>45–47</sup> The Ba 3d data (Figure 5(b)) could be modeled with a single component for the entire series, highlighting the low temperature-dependence of the chemical nature of Ba. On the other hand, the Zr 3d data (Figure 5(c)) which also includes Ba 4p<sub>3/2</sub> (shaded peak at ~179.1 eV), reveals a second contribution at slightly lower binding energies (BZS-800 and

BZS-1000). For BZS-1000, an additional Zr feature is observed, consistent with the emergence of minor oxide phases as the film decomposes.<sup>37</sup> The absence of any specific temperature trend of the Zr/Ba ratio obtained from composition analysis of the XPS data suggests that the thermal process can have distinct and complex effects on surface structure and composition. A detailed description of the composition analyses is provided in the [Supporting Information](#), which includes an overlay of survey photoemission spectra for all Ba–Zr–S thin films ([Figure S3\(a\)](#)) and the corresponding composition profiles as a function of the annealing temperature ([Figure S3\(b\)](#)); the numbers are also tabulated ([Table S6](#)). The high sensitivity of the surface is also attributed to the variable morphology of the film and the different surface oxidation effects.

The S 2p spectra reveal two distinct regions: a low-binding-energy region (ca. 160–166 eV), related to Ba–Zr–S, and a high-binding-energy region (ca. 166–171.5 eV), related to oxidized S states.<sup>48</sup> The most prominent emissions at 169.5 and 167.6 eV coincide in binding energy with the S 2p<sub>3/2</sub> of sulfate (SO<sub>4</sub><sup>2-</sup>; S(+VI)) and sulfite (SO<sub>3</sub><sup>2-</sup>; S(+IV)), the most likely assignment being BaSO<sub>4</sub> and BaSO<sub>3</sub>, respectively. These oxidized sulfur species are already formed as a result of surface oxidation upon unloading the films from the sputtering chamber, as they are also present in the precursor. The effect of the film heterogeneity is distinctly visible in [Figure 5](#), specifically with S, which adopts varied chemical environments at different annealing temperatures and yields different surface structures. Similar observations could be made for the O 1s core-level spectra ([Figure S3\(c\)](#) in the [Supporting Information](#)), which needed at least three Gaussian peaks with non-monotonic intensity variations for a proper description. The heterogeneity of the film surfaces was tested by measuring XPS on multiple spots on each film. A comparison of surface compositions estimated from two different spots on BZS-900, taken as a representative of the Ba–Zr–S films, is given in [Figure S4](#) and [Table S8](#) in the [Supporting Information](#). We mention here that since the samples are highly heterogeneous at the surface, we limited the composition estimation to using the intensity of the different core-level peaks and correcting for the cross section only. This, therefore, gives us an approximate estimate and should only be used to provide rough numbers. However, it allows us to follow trends when comparing different compounds. From the composition study, it is clear that the oxidized sulfur signature is persistent at all temperatures, establishing a strong oxidation effect in the first few monolayers (ca. 1–2 nm) of the Ba–Zr–S films.

**HAXPES.** Hard X-ray photoelectron spectroscopy (HAXPES) enables a greater sampling depth of analysis than conventional XPS. Based on the finding that the BaZrS<sub>3</sub> films of best quality were produced at an annealing temperature of 900 °C, we chose this film for further investigation. This focused on the surface oxide layer thickness and the corresponding chemical state of the components existing deep within the bulk of the film by utilizing a high photon energy of 4.0 keV. Since the film thickness was not uniform, several spots were checked for Si signals coming from the substrate. A comparison of two representative spots—one Si-rich, thinner (magenta) and one Si-poor, thicker (black), as denoted by the Si 2p signal—is provided in [Figure S5](#) in the [Supporting Information](#). All HAXPES data discussed here are related to the representative Si-poor spot.

The binding energy calibration of the HAXPES data was performed using Au 4f<sub>7/2</sub> (84.0 eV) and the Fermi level (0 eV) measured at 4.0 keV. We found that the O signal could still be detected in the HAXPES data. In [Figure 6](#), we compare the

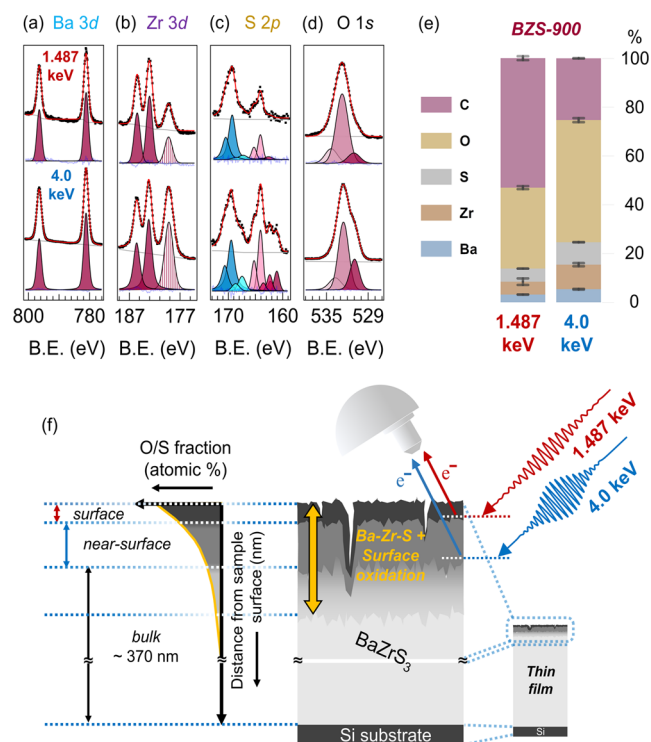


**Figure 6.** Depth-profiling using photoemission spectroscopy: data (black symbols) and fit (red) to core-level spectra of (a) Ba 3d, (b) Zr 3d, (c) S 2p, and (d) O 1s for BZS-900 film obtained using high photon energy (HAXPES@4.0 keV) compared to Al K<sub>α</sub> XPS (1.487 keV) results from [Figure 5](#). The individual components for each fit are also presented. (e) Relative fraction of Ba, Zr, S, O, and C in the BZS-900 film measured at different photon energies: Al K<sub>α</sub> (left column) and 4.0 keV (right column). (f) Schematic comparing depth sensitivities achieved for BZS-900 films using conventional (1.487 keV, dark red) and hard (4.0 keV, dark blue) X-rays.

core-level spectra of (a) Ba 3d, (b) Zr 3d, (c) S 2p, and (d) O 1s at 4.0 keV with the Al K<sub>α</sub> XPS data from [Figure 5](#). The binding energy values extracted from the 3d spectra of Ba and Zr were consistent with the Al K<sub>α</sub> XPS results, suggesting that Ba<sup>2+</sup> and Zr<sup>4+</sup> persist as the dominant species, related to orthorhombic BaZrS<sub>3</sub>. The S 2p spectra contain signatures from the perovskite structure as well as from the oxidized S states. This implies that O persists several nanometers (~5 nm) within the films. The low-binding-energy region of the S 2p spectra could be modeled by three components, of which the contribution of the doublet related to the lowest binding energy is assigned to the BaZrS<sub>3</sub> perovskite. The other two components possibly arise from Ba–Zr–S-related species closer to the surface.

As the surface contribution decreases going from Al K<sub>α</sub> to 4.0 keV, we find that the fraction of oxidized S species relative to the perovskite decreases toward the bulk of BZS-900. Nonetheless, the amount of oxidized S is still considerable. This is evident from the O 1s spectra, which reveal the presence of multiple oxygen species at the near-surface region. The peaks centered around 531.0, 532.6, and 533.9 eV are related to O<sup>2-</sup> bonded to Zr, surface O, and chemisorbed O,

respectively. For the BZS-900 film, the depth-dependent composition analysis obtained from Figure 6(a–d) is presented in Figure 6(e) and Table S10 in the Supporting Information. One can see that, with increased probing depth, the S:O ratio also increases (Table S10), suggesting less extent of oxidation deeper into the bulk of the films. This also explains why the relative contribution of the oxidized S to the total S 2p spectra (Figure 6(c)) decreases with increasing photon energies.

The clear presence of O up to a few nanometers from the surface of the films annealed at 900 °C is further aided by the poor morphology. Indeed, our reported ToF-ERDA results<sup>37</sup> showed that the O content in BZS precursors decreased smoothly up to depths of ~30 nm, which is ~8% of the overall film thickness. Considering such O-contributions in the surface region, the depth-profiling achieved here with HAXPES, therefore, represents more of a contrast between the surface and near-surface region of the film rather than a contrast between the surface and the bulk of the BZS-900 films, as represented by the schematic given in Figure 6(f).

Figure 7 compares the valence band spectra of BZS-900 thin film measured at two different photon energies: 1.487 and 4.0

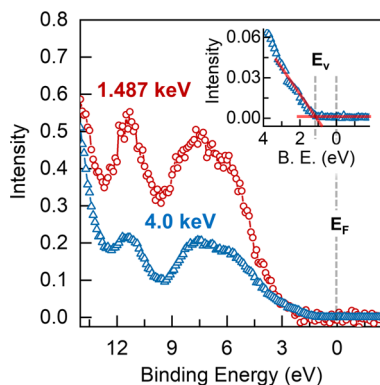


**Figure 7.** Valence band spectra for BZS-900 thin film measured at low ( $\text{Al } K_{\alpha} = 1.487 \text{ keV}$ , dark red circles) and high (4.0 keV, dark blue triangles) photon energies. The inset shows the position of the valence band edge measured at 4.0 keV.

keV; both spectra were normalized to the Ba 5p peak (~15 eV) of the survey spectra (not shown here). Specific surface chemistry contributions can lead to erroneous interpretation of the valence band and the character of its edge. Therefore, the valence band spectra obtained at 4.0 keV, due to its higher information depth, were chosen for a better estimate of the edge position ( $E_v$ ) relative to the Fermi level ( $E_F$ ):  $\Delta E = |E_F - E_v|$ . Applying a linear fit to the valence band edge, we find the  $E_v$  position to be 1.1 eV below  $E_F$  ( $\Delta E = 1.1 \text{ eV}$ ). Given that the reported band gap ( $E_g$ ) value of BZS-900 films is ~1.84 eV, our results may indicate a light  $n$ -type behavior, as also observed by Wei et al.<sup>11</sup> We note here that the observed  $\Delta E$  value shows only a small departure from an intrinsic behavior ( $\Delta E - E_g/2 \sim 0.2 \text{ eV}$ ) and such light  $n$ -type doping can also originate from subtle variation in composition or states in the surface region appearing at the valence band edge.

## DISCUSSION

Combining the results, we can arrive at a comprehensive understanding of the nature of the sputtered films in terms of

geometric structure, phase distribution, and surface electronic structure in the context of a solar cell material.

**Geometric Structure.** Figures 3 and 4 allow us to envisage the process of temperature-induced crystallization of the initially amorphous BZS precursor into crystalline  $\text{BaZrS}_3$ , and thereafter, how the crystal breaks down beyond the decomposition temperature. In the precursors, no long-range ordering was observed from XRD.<sup>37</sup> Zr  $K$ -EXAFS reveals that locally the Zr atoms assume a low S coordination (~5.2) and a relatively long Zr–S bond (~2.59 Å), indicating the structural density of BZS-pre films to be lower than a crystalline phase. In addition to S, each Zr atom also bonds to ~0.4 O atoms, which indicates the presence of O in the precursor, as also reported from bulk composition analysis using EDS and ion beam techniques (ref 37, Table 2). Due to such a highly disordered Zr–S/O<sub>n</sub> network, BZS-pre shows no perceivable Zr–Ba and Zr–Zr short-range definition. The as-deposited films, therefore, can be largely approximated as an aperiodic network of Ba, Zr, and S atoms, with minor O impurities. It is important to note that although the precursor film is amorphous, the immediate neighboring environment of the Zr atoms does attain a definition that is approximately similar to the average local environment around Zr in the annealed films (Figure 1(b)). This can be understood from the fact that the overall stoichiometry of the precursor film is close to the ideal  $\text{BaZrS}_3$  composition, as established by both IBA and EDS studies.<sup>37</sup>

Annealing provides thermal energy to the amorphous Ba–Zr–S network, which rearranges to gain long-range periodic order. After the formation temperature (650 °C) has been reached, small  $\text{BaZrS}_3$  crystallites (~10 nm, Figure 4(b)) appear, yielding Bragg reflections characteristic of an orthorhombic structure. At 700 °C, slightly larger crystallites (~13 nm) are formed. The transition from an amorphous to a dense crystalline phase is reflected in Zr  $K$ -EXAFS from BZS-pre to BZS-700, with an abrupt drop in the distribution of Zr–S distances ( $\sigma^2$ ) and shrinking of Zr–S bonds by ~0.05 Å, attaining ideal Zr–S bond lengths (2.53–2.54 Å) in the orthorhombic  $\text{BaZrS}_3$  structure (Figure 3). The corresponding Zr–S/O<sub>n</sub> environment reveals an increased number of S bonds to Zr (~5.4) with no discernible signature of O bonds to Zr. The Ba–Zr–S films annealed at low temperatures (650–700 °C), therefore, comprise primarily small  $\text{BaZrS}_3$  perovskite crystallites, alongside Zr–O-rich and Ba–S-rich areas. With a further increase of the annealing temperature to 800–900 °C,  $\text{BaZrS}_3$  crystallites grow in size (~20 nm) and the crystallinity improves, as evidenced by narrowing of the [121] Bragg peaks in XRD (Figure 4(b)). At the local scale, EXAFS reveals that S attains a 6-fold coordination with Zr, characteristic of the perovskite B site (Figure 3(a)). The average Zr–S distances remain similar to BZS-700, with the S environment attaining a minimum  $\sigma^2$  in the temperature range of 800–900 °C. The width of [121] Bragg reflection ( $[121]_{\text{FWHM}}$ , Figure 4(b)) reflects the effective thickness of the [121] crystallographic plane, while the Zr–S  $\sigma^2$  (Figure 3(c)) in EXAFS reflects the variance of the mean Zr–S bond length, both of which are linked to the degree of crystallinity of  $\text{BaZrS}_3$ . The strong resemblance of temperature evolution between  $[121]_{\text{FWHM}}$  and Zr–S  $\sigma^2$  values, therefore, reflects how the temperature-induced crystallization and growth process of  $\text{BaZrS}_3$  is tracked at complementary global and local structural length scales.<sup>49</sup>

The position of the [121] Bragg peak remains similar, regardless of the choice of annealing temperature ( $2\theta \sim 25.3^\circ$ ; see Table S4, Supporting Information). This indicates that

when perovskite crystallites of BaZrS<sub>3</sub> as small as ~10 nm are formed at 650 °C, they already attain ideal lattice parameters for an orthorhombic structure. The average BaZrS<sub>3</sub> unit cell dimensions thereafter remain constant upon annealing, while the crystallites grow and the films attain higher crystallinity. A more regular arrangement of the three-dimensional lattice also makes higher NN shell features related to Zr–Ba and Zr–Zr correlations visible in the Zr *K*- $\chi(R)$  functions (Figure 2(a)). Although small crystallite sizes render quantification of Zr–Ba and Zr–Zr peaks a bit difficult in EXAFS, our higher NN shell fits to BZS-900 and BZS-1000 reveal the average Zr–Ba and Zr–Zr interatomic distances to be similar to the reported polycrystalline bulk orthorhombic BaZrS<sub>3</sub>.<sup>21</sup> Nonetheless,  $\chi(R)$  perfectly tracks the formation and growth mechanism of BaZrS<sub>3</sub> crystallites within the Ba–Zr–S films. We note here that the structural parameters extracted from XRD and EXAFS both indicate that the S environments obtained in the films annealed at 800 and 900 °C are rather comparable. The true advantage of the BZS-900 film lies in its improved crystallinity and larger crystallite size (Figure 4(b)) which reduce grain boundary effects, both of which are crucial in terms of optical properties, as discussed in the subsequent sections.

The XRD analyses reveal that the position of the [121] Bragg peak remains constant at ( $2\theta \sim 25.3^\circ$ , see Table S4, Supporting Information) over the entire temperature range (650–1000 °C). Also, no discernible signature of O bonded to Zr could be established from EXAFS for BZS-700, BZS-800, and BZS-900. Both observations imply that the observed small crystallites are not of BaZrS<sub>3</sub>–BaZrO<sub>3</sub> solid solutions.<sup>50</sup> Rather, these are pure BaZrS<sub>3</sub> crystallites that grow from the amorphous phase by expelling O from the perovskite lattice. During the thermal process, O also crystallizes predominantly as ZrO<sub>2</sub>, as identified in XRD and STEM-EDS.<sup>37</sup> Due to the higher concentration and larger atomic scattering factor of S compared to that of O, Zr–O correlations from minor oxide phases of ZrO<sub>2</sub> are not captured properly in the Zr *K*-EXAFS in the temperature range 700–900 °C. The Zr–O correlations reappear at 1000 °C when the film degrades, producing additional oxide and sulfide phases.

**Phase Distribution.** The freshly sputtered films, upon unloading from the sputter chamber, immediately react with atmospheric O<sub>2</sub>. Consequently, exposure to air leads to some S loss, especially from the S-rich phases of the film surface.<sup>37</sup> PES detects strong composition fluctuations due to the formation of several new chemical species of S related to the perovskite, binary S phases and oxidized S (e.g., BaSO<sub>3</sub>, BaSO<sub>4</sub>), as well as O species including ZrO<sub>2</sub> (possibly Ba–O), and chemisorbed O. ToF-ERDA results<sup>37</sup> confirm that the O content is highest at the surface (~20%), with only ca. 3–4% occurring in the bulk of the BZS-pre films. The oxidized species detected from PES are, therefore, mostly limited toward the film surface and near-surface regions, while the bulk Ba/Zr/S composition remains close to the 1:1:3 perovskite stoichiometry.

Rapid thermal processing induces the BaZrS<sub>3</sub> perovskite crystallization, as validated by XRD, with further S loss and a modest increase of O content, detected by EDS.<sup>37</sup> This is aided by the generation of cracks and pinholes, leading to additional surface oxidation in the annealed films. Both effects lead to phase redistributions, the effects of which are strongest at the surface of the annealed films. This is evident from our depth-dependent PES studies on the BZS-900 film, which revealed a lower S:O ratio at the film surface (1.487 keV) compared to the near-surface region (4.0 keV) (Supporting

Information, Table S10). Trends in the temperature dependence of the film surface composition from XPS studies are less clear. Rather, each film adopts a different stoichiometry due to varying fractions of several O and S species.

Interestingly, while EDS revealed a decrease in S content and an increase in O content after annealing,<sup>37</sup> EXAFS reveals an opposite trend, with an increase in the average coordination of S to Zr, and almost undetected O coordination within the perovskite structure. This is predominantly related to different annealing-induced phase distributions for the S and O. S participates in the crystallization process of BaZrS<sub>3</sub> from an amorphous phase at relatively low temperatures (650 °C). Subsequently, the crystallites grow over the entire thermal process up to 900 °C. One can therefore suggest that an overall perovskite stoichiometry is achieved in the annealed films, and the Zr atoms predominantly constitute the desired orthorhombic BaZrS<sub>3</sub> phase. The remaining fraction of Zr primarily occurs in Zr–O-rich areas in the amorphous precursor film and mostly forms the minor secondary phase ZrO<sub>2</sub>. Similar observations were made in Eu doping in ZnO nanosponges, where molecular Eu–O clusters embedded in hexagonal ZnO crystallites of similar dimensions (ca. 10–20 nm) precipitate out of the ZnO lattice when annealed.<sup>51</sup>

Our description of annealing-induced phase distribution in Ba–Zr–S thin films closely resembles the chemical inhomogeneity captured by STEM-EDS spectral imaging of the BZS-900 film, which clearly revealed areas of the film containing Zr- and O-rich zones, which are Ba and S-deficient (ref 37, Figure 7). When BaZrS<sub>3</sub> crystallites grow in size with increasing annealing temperature, one expects ZrO<sub>2</sub> and other secondary oxide and sulfide phases to be redistributed more toward crystallite boundaries, which eventually emerge out of the film upon further annealing (1000 °C).<sup>37</sup>

The persistence of a small amount of O in the Ba–Zr–S films highlights the susceptibility of the Ba–Zr–S precursors to oxidation. This is not surprising, considering the higher reactivity of O<sup>2-</sup> toward the metals compared to S<sup>2-</sup>, particularly smaller Zr<sup>4+</sup> with a higher charge density than Ba<sup>2+</sup>. Highly electronegative and weakly polarizable O<sup>2-</sup> would act as a hard Lewis base that would preferably bind with the hard Lewis acid Zr<sup>4+</sup>. The interaction with O has stronger effects on the chemical nature of Zr, yielding additional binding configurations. The larger Ba<sup>2+</sup> ion, on the other hand, typically resides in a large coordination environment with less pronounced chemical effects. Nonetheless, the binding of some O to Ba cannot be ruled out completely.

**Electronic Properties.** The results from our structural data offer a more detailed explanation of the photoluminescence (PL) data (Figure 8(a)), reproduced from our previous paper<sup>37</sup> on Ba–Zr–S thin films annealed at different temperatures. The corresponding structure–function relation diagram is shown in Figure 8(b), where we replot the temperature evolution of Zr–S  $\sigma^2$  from EXAFS (bottom panel, same as Figure 3(c)) and [121]<sub>FWHM</sub> from XRD (middle panel, same as Figure 4(b)), and compare them to the temperature evolution of the PL maxima (PL<sub>max</sub>) and FWHM (PL<sub>FWHM</sub>) (reproduced from our previous paper<sup>37</sup>). For the case of 700 °C, the film shows significant defect emission at low energies ~1.6 eV. With annealing, the dominant BaZrS<sub>3</sub> phase grows and the fraction of minor impurity phases (e.g., Zr–O-rich regions) shrinks, leading to dampening of the PL intensities at low photon energies. The main PL signal, on the other hand, gains intensity (cyan open circles; top panel in Figure 8(b),

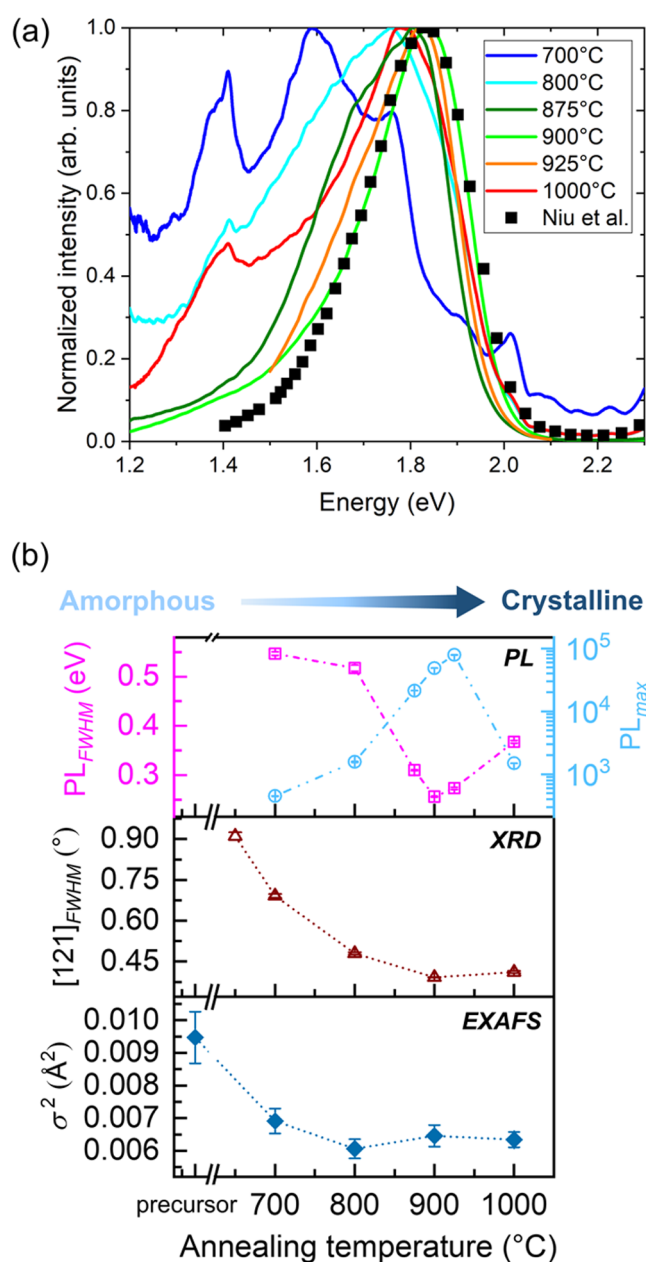


**Figure 8.** (a) Normalized photoluminescence (PL) from samples annealed at different temperatures. (b) Correlation between evolution of maximum intensity and FWHM (top panel) of the PL curves shown in (a), FWHM of [121] Bragg reflection from XRD (middle panel), and Zr–S  $\sigma^2$  values from EXAFS (bottom panel). Panel (a) and top panel of (b) were reproduced from ref 37 under the Creative Commons license CC BY 4.0. The data of Niu et al. used in the preparation of the original figure was digitized from ref 12 (Niu et al. *Adv. Mater* (2017)).

right axis) following the BaZrS<sub>3</sub> crystallite growth profile (black open circles, Figure 4(b)) and lowering disorder in the Zr local environment (dark blue closed diamonds; lower panel in Figure 8(b)). The film crystallinity simultaneously improves (dark red open triangles, middle panel in Figure 8(b)), leading to narrowing of the main PL signal (magenta open squares, top panel in Figure 8(b), left axis). The PL peak systematically shifts to higher energies with annealing, eventually conforming to the reported bulk optical band gap value of 1.84 eV. Since this value was achieved for the thin films annealed at 900 °C,

which also exhibited the highest degree of crystallinity, the optimal annealing temperature utilizing this synthesis method was concluded to be 900 °C. Increasing the annealing temperature any further adversely affected the trend, as evident from the abrupt lowering of the PL intensity, broadening of the main PL peak, and emergence of lower energy features (Figure 8(a)). Figure 8(b) shows how the corresponding FWHM values extracted from the main PL peak (open squares; magenta) reveal a strong resemblance to the evolution of [121]<sub>FWHM</sub> from XRD data (wine open triangles, same as Figure 4(b)) and Zr–S  $\sigma^2$  values from EXAFS data (dark blue closed diamonds, same as Figure 3(c)). This observation highlights how optical properties can be traced down to atomic-scale<sup>52</sup> structural changes in the films induced by temperature. Controlled structural modifications by tuning synthesis parameters, therefore, are a viable approach to band gap engineering in BaZrS<sub>3</sub>.

The structure–function correlation observed in Figure 8(b) for the sputtered BaZrS<sub>3</sub> thin films annealed at 900 °C is rather bulk in nature and is relatively less affected by surface oxidation effects. While the BZS-900 film possesses good crystallinity and a band gap expected for bulk BaZrS<sub>3</sub>, it is important to realize that the films are still polycrystalline in nature with an average crystallite size of  $\sim 22 \pm 0.1$  nm. At such small sizes, grain boundary effects are still operative. Also, the films contain minor disordered oxide phases with higher contributions at the surface. Such factors could be detrimental to the optoelectronic properties. Given that the optical gap of BZS-900 is 1.84 eV, our estimation of the valence band edge position would suggest the film to be *n*-type. However, due to the above-mentioned factors, one cannot rule out the possibility that such surface contributions might interfere with the accuracy of the estimated edge position of the valence band relative to the Fermi level. A more precise estimation of the position of the valence band edge relative to the Fermi level of the ideal BaZrS<sub>3</sub> material could be concluded from single-crystalline<sup>19,21</sup> BaZrS<sub>3</sub>, which we are currently focusing on, alongside alternative synthesis strategies that require lower annealing temperatures<sup>33,53</sup> and are more compatible with solar cell integration processes.

## CONCLUSIONS

We have investigated the first reported sputtered thin films of BaZrS<sub>3</sub> in terms of local and global geometric structures, phase distribution, and surface and near-surface chemical and electronic structures. The study follows how freshly sputtered Ba–Zr–S precursor films evolve from amorphous to crystalline BaZrS<sub>3</sub> phase and how the annealing temperature affects such formation mechanisms. Due to the presence of S-rich phases and nonuniform surface deposition, amorphous BZS precursors undergo immediate surface oxidation upon air exposure. Once a thermal process is initiated, small orthorhombic BaZrS<sub>3</sub> perovskite units crystallize from the amorphous matrix. Further annealing leads to significant crystallite growth until a temperature of 900 °C, where films attain a narrow photoluminescence peak and an optical band gap of 1.84 eV, similar to that of an ideal bulk. The minor secondary phase is comprised primarily of Zr–O-rich regions, which do not seem to participate in the crystallization and growth process of BaZrS<sub>3</sub>, but rather largely precipitate out at higher temperatures as a secondary ZrO<sub>2</sub> phase. Our surface material chemistry investigation utilizing photoemission spectroscopy reveals most of the O to be confined to the film

surface, while some of the O reacts several nanometers into the film and forms minor Zr–O-rich regions that are distributed heterogeneously near the surface of the amorphous film matrix. Nevertheless, beneath the surface oxide layer, the bulk of the 900 °C film comprises predominantly of BaZrS<sub>3</sub> perovskite. Based on the results of our measured band gap and position of the Fermi level, we assign the semiconductor material to be close to intrinsic with a slight *n*-type character. The observed PL data could be directly linked to the phase distribution information, which complements the global structural information obtained from BaZrS<sub>3</sub> crystallite growth and improved crystallinity, down to atomic-scale information on Zr–S bonding arrangements and  $\sigma^2$  values. Our insights into the nature of this semiconductor, with electronic properties that can be controlled through structural modifications, is key toward utilizing such films in photovoltaic applications.

## ■ ASSOCIATED CONTENT

### SI Supporting Information

The Supporting Information is available free of charge at <https://pubs.acs.org/doi/10.1021/acsaem.3c02075>.

Details of data analyses for: I. X-ray absorption spectroscopy/extended X-ray absorption fine structure (XAS/EXAFS), II. X-ray diffraction (XRD), III. Photoelectron spectroscopy (conventional: XPS/Hard X-rays: HAXPES); Figures S1 and S2: EXAFS fits to BaZrS<sub>3</sub> thin films; Figures S3–S5: composition analyses from PES using conventional Al K <sub>$\alpha$</sub>  (1.487 keV) and hard X-rays (4.0 keV); Tables S1–S3: parameters extracted from EXAFS analyses; Table S4: parameters extracted from XRD analyses; Tables S5–S10: parameters extracted from PES analyses (PDF)

## ■ AUTHOR INFORMATION

### Corresponding Authors

**Soham Mukherjee** – Condensed Matter Physics of Energy Materials, Division of X-ray Photon Science, Department of Physics and Astronomy, Uppsala University, SE-75120 Uppsala, Sweden; [orcid.org/0000-0002-3656-7207](https://orcid.org/0000-0002-3656-7207); Email: [soham.mukherjee@physics.uu.se](mailto:soham.mukherjee@physics.uu.se), [soham.chem@gmail.com](mailto:soham.chem@gmail.com)

**Håkan Rensmo** – Condensed Matter Physics of Energy Materials, Division of X-ray Photon Science, Department of Physics and Astronomy, Uppsala University, SE-75120 Uppsala, Sweden; [orcid.org/0000-0001-5949-0997](https://orcid.org/0000-0001-5949-0997); Email: [hakan.rensmo@physics.uu.se](mailto:hakan.rensmo@physics.uu.se)

### Authors

**Stefania Riva** – Condensed Matter Physics of Energy Materials, Division of X-ray Photon Science, Department of Physics and Astronomy, Uppsala University, SE-75120 Uppsala, Sweden; [orcid.org/0000-0001-8449-1166](https://orcid.org/0000-0001-8449-1166)

**Corrado Comparotto** – Division of Solar Cell Technology, Department of Materials Science and Engineering, Uppsala University, Uppsala 75237, Sweden; [orcid.org/0000-0002-6020-0771](https://orcid.org/0000-0002-6020-0771)

**Fredrik O. L. Johansson** – Institute Methods and Instrumentation for Synchrotron Radiation Research PS-ISR, Helmholtz-Zentrum Berlin für Materialien und Energie, 12489 Berlin, Germany; Institut für Physik und Astronomie, Universität Potsdam, 14476 Potsdam, Germany; Present Address: Division of Applied Physical Chemistry,

Department of Chemistry, KTH – Royal Institute of Technology, SE-100 44 Stockholm, Sweden; [orcid.org/0000-0002-6471-1093](https://orcid.org/0000-0002-6471-1093)

**Gabriel J. Man** – Condensed Matter Physics of Energy Materials, Division of X-ray Photon Science, Department of Physics and Astronomy, Uppsala University, SE-75120 Uppsala, Sweden; Present Address: MAX IV Laboratory, Lund University, PO Box 118, Lund 221 00, Sweden; [orcid.org/0000-0003-2932-7018](https://orcid.org/0000-0003-2932-7018)

**Dibya Phuyal** – Division of Material and Nano Physics, Department of Applied Physics, KTH Royal Institute of Technology, Stockholm 10691, Sweden; [orcid.org/0000-0003-0351-3138](https://orcid.org/0000-0003-0351-3138)

**Konstantin A. Simonov** – Department of Materials and Process Development, Swerim AB, SE-164 07 Kista, Sweden

**Justus Just** – MAX IV Laboratory, Lund University, 22100 Lund, Sweden

**Konstantin Klementiev** – MAX IV Laboratory, Lund University, 22100 Lund, Sweden; [orcid.org/0000-0002-9468-4188](https://orcid.org/0000-0002-9468-4188)

**Sergei M. Butorin** – Condensed Matter Physics of Energy Materials, Division of X-ray Photon Science, Department of Physics and Astronomy, Uppsala University, SE-75120 Uppsala, Sweden; [orcid.org/0000-0003-3242-5305](https://orcid.org/0000-0003-3242-5305)

**Jonathan J. S. Scragg** – Division of Solar Cell Technology, Department of Materials Science and Engineering, Uppsala University, Uppsala 75237, Sweden; [orcid.org/0000-0001-8686-8721](https://orcid.org/0000-0001-8686-8721)

Complete contact information is available at: <https://pubs.acs.org/doi/10.1021/acsaem.3c02075>

### Author Contributions

The manuscript was written through contributions of all authors. All authors have given approval to the final version of the manuscript.

### Notes

The authors declare no competing financial interest.

## ■ ACKNOWLEDGMENTS

The authors gratefully acknowledge STandUP for Energy, the National Strategic e-Science Program eSENCE, the Swedish Research Council (grant nos. VR 2017-04341, 2018-06465, and 2018-04330), the Swedish Foundation for Strategic Research (project no. RMA15-0130), and the Swedish Energy Agency (grant no. P43549-1, P50626-1) for financial support. S.M.B acknowledges the support from the Swedish Research Council (research grant 2018-05525). D.P. acknowledges Swedish Research Council (research grant 2020-00681). J.S. and C.C. gratefully acknowledge the Göran Gustafsson Foundation (grant no. 1927), the Swedish Research Council (2017-04336), for funding this research, and Myfab Uppsala for providing facilities and experimental support. Myfab is funded by the Swedish Research Council (2019-00207) as a national research infrastructure. In addition, we acknowledge MAX IV Laboratory for time on Beamline Balder under Proposal 20200413. Research conducted at MAX IV, a Swedish national user facility, is supported by the Swedish Research Council under contract 2018-07152, the Swedish Governmental Agency for Innovation Systems under contract 2018-04969, and Formas under contract 2019-02496.

## ■ ABBREVIATIONS

XAS, X-ray absorption spectroscopy; XANES, X-ray absorption near-edge spectroscopy; EXAFS, extended X-ray absorption fine structure spectroscopy; XRD, X-ray diffraction; PES, Photoelectron Spectroscopy; XPS, X-ray Photoelectron Spectroscopy; HAXPES, Hard X-ray Photoelectron Spectroscopy; BZS, BaZrS<sub>3</sub>; BZS-pre, sputtered Ba–Zr–S precursor film; BZS-650, thin film annealed at 650 °C; BZS-700, thin film annealed at 700 °C; BZS-800, thin film annealed at 800 °C; BZS-900, thin film annealed at 900 °C; BZS-1000, thin film annealed at 1000 °C

## ■ REFERENCES

- (1) Hahn, V. H.; Frank, G.; Klingler, W.; Meyer, A.-D.; Ströger, G. Untersuchungen Über Ternäre Chalkogenide. *Z. Anorg. Allg. Chem.* **1957**, *288*, 269–278.
- (2) Clearfield, A. The Synthesis and Crystal Structures of Some Alkaline Earth Titanium and Zirconium Sulfides. *Acta Crystallogr.* **1963**, *16*, 135–142.
- (3) Filippone, S.; Zhao, B.; Niu, S.; Koocher, N. Z.; Silevitch, D.; Fina, I.; Rondinelli, J. M.; Ravichandran, J.; Jaramillo, R. Discovery of Highly Polarizable Semiconductors BaZrS<sub>3</sub> and Ba<sub>3</sub>Zr<sub>2</sub>S<sub>7</sub>. *Phys. Rev. Mater.* **2020**, *4*, No. 091601.
- (4) Adjogri, S. J.; Meyer, E. L. Chalcogenide Perovskites and Perovskite-Based Chalcogenide as Photoabsorbers: A Study of Their Properties, and Potential Photovoltaic Applications. *Materials* **2021**, *14*, 7857.
- (5) Sun, Y. Y.; Agiorgousis, M. L.; Zhang, P.; Zhang, S. Chalcogenide Perovskites for Photovoltaics. *Nano Lett.* **2015**, *15*, 581–585.
- (6) Sopiha, K. V.; Comparotto, C.; Márquez, J. A.; Scragg, J. J. S. Chalcogenide Perovskites: Tantalizing Prospects, Challenging Materials. *Adv. Opt. Mater.* **2022**, *10*, No. 2101704.
- (7) Osei-Agyemang, E.; Koratkar, N.; Balasubramanian, G. Examining the Electron Transport in Chalcogenide Perovskite BaZrS<sub>3</sub>. *J. Mater. Chem. C* **2021**, *9*, 3892–3900.
- (8) Osei-Agyemang, E.; Adu, C. E.; Balasubramanian, G. Ultralow Lattice Thermal Conductivity of Chalcogenide Perovskite CaZrSe<sub>3</sub> Contributes to High Thermoelectric Figure of Merit. *npj Comput. Mater.* **2019**, *5*, No. 116.
- (9) Jena, A. K.; Kulkarni, A.; Miyasaka, T. Halide Perovskite Photovoltaics: Background, Status, and Future Prospects. *Chem. Rev.* **2019**, *119*, 3036–3103.
- (10) Snaith, H. J. Present Status and Future Prospects of Perovskite Photovoltaics. *Nat. Mater.* **2018**, *17*, 372–376.
- (11) Wei, X.; Hui, H.; Zhao, C.; Deng, C.; Han, M.; Yu, Z.; Sheng, A.; Roy, P.; Chen, A.; Lin, J.; Watson, D. F.; Sun, Y. Y.; Thomay, T.; Yang, S.; Jia, Q.; Zhang, S.; Zeng, H. Realization of BaZrS<sub>3</sub> Chalcogenide Perovskite Thin Films for Optoelectronics. *Nano Energy* **2020**, *68*, No. 104317.
- (12) Niu, S.; Huyan, H.; Liu, Y.; Yeung, M.; Ye, K.; Blankemeier, L.; Orvis, T.; Sarkar, D.; Singh, D. J.; Kapadia, R.; Ravichandran, J. Bandgap Control via Structural and Chemical Tuning of Transition Metal Perovskite Chalcogenides. *Adv. Mater.* **2017**, *29*, No. 1604733.
- (13) Song, Z.; Chen, C.; Li, C.; Awni, R. A.; Zhao, D.; Yan, Y. Wide-Bandgap, Low-Bandgap, and Tandem Perovskite Solar Cells. *Semicond. Sci. Technol.* **2019**, *34*, No. 093001.
- (14) Werner, J.; Niesen, B.; Ballif, C. Perovskite/Silicon Tandem Solar Cells: Marriage of Convenience or True Love Story? – An Overview. *Adv. Mater. Interfaces* **2018**, *5*, No. 1700731.
- (15) Huo, Z.; Wei, S. H.; Yin, W. J. High-Throughput Screening of Chalcogenide Single Perovskites by First-Principles Calculations for Photovoltaics. *J. Phys. D: Appl. Phys.* **2018**, *51*, No. 474003.
- (16) Meng, W.; Saporov, B.; Hong, F.; Wang, J.; Mitzi, D. B.; Yan, Y. Alloying and Defect Control within Chalcogenide Perovskites for Optimized Photovoltaic Application. *Chem. Mater.* **2016**, *28*, 821–829.
- (17) Bennett, J. W.; Grinberg, I.; Rappe, A. M. Effect of Substituting of S for O: The Sulfide Perovskite BaZrS<sub>3</sub> Investigated with Density Functional Theory. *Phys. Rev. B* **2009**, *79*, No. 235115.
- (18) Nishigaki, Y.; Nagai, T.; Nishiwaki, M.; Aizawa, T.; Kozawa, M.; Hanzawa, K.; Kato, Y.; Sai, H.; Hiramatsu, H.; Hosono, H.; Fujiwara, H. Extraordinary Strong Band-Edge Absorption in Distorted Chalcogenide Perovskites. *Sol. RRL* **2020**, *4*, No. 1900555.
- (19) Li, W.; Niu, S.; Zhao, B.; Haiges, R.; Zhang, Z.; Ravichandran, J.; Janotti, A. Band Gap Evolution in Ruddlesden-Popper Phases. *Phys. Rev. Mater.* **2019**, *3*, No. 101601.
- (20) Phuyal, D.; Mukherjee, S.; Panda, S. K.; Jana, S.; Segre, C. U.; Simonelli, L.; Butorin, S. M.; Rensmo, H.; Karis, O. Origin of Itinerant Carriers in Antiferromagnetic LaFe<sub>1-x</sub>Mo<sub>x</sub>O<sub>3</sub> Studied by x-Ray Spectroscopies. *Phys. Rev. Mater.* **2020**, *4*, No. 034405.
- (21) Niu, S.; Zhao, B.; Ye, K.; Bianco, E.; Zhou, J.; McConney, M. E.; Settens, C.; Haiges, R.; Jaramillo, R.; Ravichandran, J. Crystal Growth and Structural Analysis of Perovskite Chalcogenide BaZrS<sub>3</sub> and Ruddlesden-Popper Phase Ba<sub>3</sub>Zr<sub>2</sub>S<sub>7</sub>. *J. Mater. Res.* **2019**, *34*, 3819–3826.
- (22) Lelieveld, R.; Ijdo, D. J. W. Sulphides with the GdFeO<sub>3</sub> Structure. *Acta Crystallogr., Sect. B: Struct. Sci., Cryst. Eng. Mater.* **1980**, *36*, 2223–2226.
- (23) Gupta, T.; Ghoshal, D.; Yoshimura, A.; Basu, S.; Chow, P. K.; Lakhnot, A. S.; Pandey, J.; Warrender, J. M.; Efstathiadis, H.; Soni, A.; Osei-Agyemang, E.; Balasubramanian, G.; Zhang, S.; Shi, S. F.; Lu, T. M.; Meunier, V.; Koratkar, N. An Environmentally Stable and Lead-Free Chalcogenide Perovskite. *Adv. Funct. Mater.* **2020**, *30*, No. 2001387.
- (24) Niu, S.; Milam-Guerrero, J.; Zhou, Y.; Ye, K.; Zhao, B.; Melot, B. C.; Ravichandran, J. Thermal Stability Study of Transition Metal Perovskite Sulfides. *J. Mater. Res.* **2018**, *33*, 4135–4143.
- (25) Gross, N.; Sun, Y. Y.; Perera, S.; Hui, H.; Wei, X.; Zhang, S.; Zeng, H.; Weinstein, B. A. Stability and Band-Gap Tuning of the Chalcogenide Perovskite BaZrS<sub>3</sub> in Raman and Optical Investigations at High Pressures. *Phys. Rev. Appl.* **2017**, *8*, No. 044014.
- (26) Perera, S.; Hui, H.; Zhao, C.; Xue, H.; Sun, F.; Deng, C.; Gross, N.; Milleville, C.; Xu, X.; Watson, D. F.; Weinstein, B.; Sun, Y. Y.; Zhang, S.; Zeng, H. Chalcogenide Perovskites - an Emerging Class of Ionic Semiconductors. *Nano Energy* **2016**, *22*, 129–135.
- (27) Wei, X.; Hui, H.; Perera, S.; Sheng, A.; Watson, D. F.; Sun, Y. Y.; Jia, Q.; Zhang, S.; Zeng, H. Ti-Alloying of BaZrS<sub>3</sub> Chalcogenide Perovskite for Photovoltaics. *ACS Omega* **2020**, *5*, 18579–18583.
- (28) Yu, Z.; Deng, C.; Kong, S.; Hui, H.; Guo, J.; Zhao, Q.; Tian, F.; Zhou, C.; Zhang, Y.; Yang, S.; Zeng, H. Transition Metal-Doped Chalcogenide Perovskite Magnetic Semiconductor BaZrS<sub>3</sub>. *J. Magn. Magn. Mater.* **2022**, *563*, No. 169886.
- (29) Zitouni, H.; Tahiri, N.; El Bounagui, O.; Ez-Zahraouy, H. Electronic, Optical and Transport Properties of Perovskite BaZrS<sub>3</sub> Compound Doped with Se for Photovoltaic Applications. *Chem. Phys.* **2020**, *538*, No. 110923.
- (30) Li, Y.; Singh, D. J. Tunability of Electronic and Optical Properties of the Ba-Zr-S System via Dimensional Reduction. *Eur. Phys. J. B* **2018**, *91*, No. 188.
- (31) Phuyal, D.; Mukherjee, S.; Jana, S.; Denoel, F.; Kamalakar, M. V.; Butorin, S. M.; Kalaboukhov, A.; Rensmo, H.; Karis, O. Ferroelectric Properties of BaTiO<sub>3</sub> Thin Films Co-Doped with Mn and Nb. *AIP Adv.* **2019**, *9*, No. 095207.
- (32) Pandey, J.; Ghoshal, D.; Dey, D.; Gupta, T.; Taraphder, A.; Koratkar, N.; Soni, A. Local Ferroelectric Polarization in Antiferroelectric Chalcogenide Perovskite BaZrS<sub>3</sub> Thin Films. *Phys. Rev. B* **2020**, *102*, No. 205308.
- (33) Comparotto, C.; Ström, P.; Donzel-Gargand, O.; Kubart, T.; Scragg, J. J. S. Synthesis of BaZrS<sub>3</sub> Perovskite Thin Films at a Moderate Temperature on Conductive Substrates. *ACS Appl. Energy Mater.* **2022**, *5*, 6335–6343.
- (34) Wang, Y.; Sato, N.; Fujino, T. Synthesis of BaZrS<sub>3</sub> by Short Time Reaction at Lower Temperatures. *J. Alloys Compd.* **2001**, *327*, 104–112.

- (35) Wang, Y.; Sato, N.; Yamada, K.; Fujino, T. Synthesis of BaZrS<sub>3</sub> in the Presence of Excess Sulfur. *J. Alloys Compd.* **2000**, *311*, 214–223.
- (36) Yan, J.; Greenblatt, M.; Sahiner, A.; Sills, D.; Croft, M. Ruddlesden-Popper Zirconium Sulfides—a Novel Preparation Method and Characterization of Electronic Structure. *J. Alloys Compd.* **1995**, *229*, 216–222.
- (37) Comparotto, C.; Davydova, A.; Ericson, T.; Riekehr, L.; Moro, M. V.; Kubart, T.; Scragg, J. Chalcogenide Perovskite BaZrS<sub>3</sub>: Thin Film Growth by Sputtering and Rapid Thermal Processing. *ACS Appl. Energy Mater.* **2020**, *3*, 2762–2770.
- (38) Klementiev, K.; Norén, K.; Carlson, S.; Sigfridsson Clauss, K. G. V.; Persson, I. The BALDER Beamline at the MAX IV Laboratory. *J. Phys. Conf. Ser.* **2016**, *712*, No. 012023.
- (39) Booth, C. H.; Bridges, F. Improved Self-Absorption Correction for Fluorescence Measurements of Extended x-Ray Absorption Fine-Structure. *Phys. Scr.* **2005**, *T115*, 202–204.
- (40) Ravel, B.; Newville, M. ATHENA, ARTEMIS, HEPHAESTUS: Data Analysis for X-Ray Absorption Spectroscopy Using IFEFFIT. *J. Synchrotron Radiat.* **2005**, *12*, 537–541.
- (41) Zabinsky, S. I.; Rehr, J. J.; Ankudinov, A.; Albers, R. C.; Eller, M. J. Multiple-Scattering Calculations of x-Ray-Absorption Spectra. *Phys. Rev. B* **1995**, *52*, 2995.
- (42) Schäfers, F. The Crystal Monochromator Beamline KMC-1 at BESSY II. *J. Large-Scale Res. Facil. JLSRF* **2016**, *2*, A96.
- (43) Dura, O. J.; Boada, R.; López De La Torre, M. A.; Aquilanti, G.; Rivera-Calzada, A.; Leon, C.; Chaboy, J. XANES and EXAFS Study of the Local Order in Nanocrystalline Ytria-Stabilized Zirconia. *Phys. Rev. B* **2013**, *87*, No. 174109.
- (44) Finkeldei, S.; Stennett, M. C.; Kowalski, P. M.; Ji, Y.; De Visser-Týnová, E.; Hyatt, N. C.; Bosbach, D.; Brandt, F. Insights into the Fabrication and Structure of Plutonium Pyrochlores. *J. Mater. Chem. A* **2020**, *8*, 2387–2403.
- (45) Jiang, L. L.; Tang, X. G.; Kuang, S. J.; Xiong, H. F. Surface Chemical States of Barium Zirconate Titanate Thin Films Prepared by Chemical Solution Deposition. *Appl. Surf. Sci.* **2009**, *255*, 8913–8916.
- (46) Zhou, H.; Mao, Y.; Wong, S. S. Shape Control and Spectroscopy of Crystalline BaZrO<sub>3</sub> Perovskite Particles. *J. Mater. Chem.* **2007**, *17*, 1707–1713.
- (47) Fuenzalida, V. M.; Pilleux, M. E. Hydrothermally Grown BaZrO<sub>3</sub> Films on Zirconium Metal: Microstructure, x-Ray Photoelectron Spectroscopy, and Auger Electron Spectroscopy Depth Profiling. *J. Mater. Res.* **1995**, *10*, 2749–2754.
- (48) Schmitz, P. J. Characterization of the Surface of BaSO<sub>4</sub> Powder by XPS. *Surf. Sci. Spectra* **2001**, *8*, 195–199.
- (49) Mukherjee, S.; Nag, A.; Kocovski, V.; Santra, P. K.; Balasubramanian, M.; Chattopadhyay, S.; Shibata, T.; Schaefer, F.; Ruz, J.; Gerard, C.; Eriksson, O.; Segre, C. U.; Sarma, D. D. Microscopic Description of the Evolution of the Local Structure and an Evaluation of the Chemical Pressure Concept in a Solid Solution. *Phys. Rev. B* **2014**, *89*, No. 224105.
- (50) Ramanandan, S. P.; Giunto, A.; Stutz, E. Z.; Reynier, B.; Lefevre, I. T. F. M.; Rusu, M.; Schorr, S.; Unold, T.; Fontuberta, I.; Morral, A.; Márquez, J. A.; Dimitrievska, M. Understanding the Growth Mechanism of BaZrS<sub>3</sub> Chalcogenide Perovskite Thin Films from Sulfurized Oxide Precursors. *J. Phys. Energy* **2023**, *5*, No. 014013.
- (51) Mukherjee, S.; Katea, S. N.; Rodrigues, E. M.; Segre, C. U.; Hemmer, E.; Broqvist, P.; Rensmo, H.; Westin, G. Entrapped Molecule-Like Europium-Oxide Clusters in Zinc Oxide with Nearly Unaffected Host Structure. *Small* **2022**, *19*, No. 2203331.
- (52) Mukherjee, S.; Phuyal, D.; Segre, C. U.; Das, S.; Karis, O.; Edvinsson, T.; Rensmo, H. Structure and Electronic Effects from Mn and Nb Co-Doping for Low Band Gap BaTiO<sub>3</sub> Ferroelectrics. *J. Phys. Chem. C* **2021**, *125*, 14910–14923.
- (53) Yang, R.; Jess, A. D.; Fai, C.; Hages, C. J. Low-Temperature, Solution-Based Synthesis of Luminescent Chalcogenide Perovskite BaZrS<sub>3</sub> Nanoparticles. *J. Am. Chem. Soc.* **2022**, *144*, 15928–15931.